JOURNAL OF AIRCRAFT
Vol. 32, No. 1, January–February 1995

Aerodynamic Characteristics of External Store Configurations at Low Speeds

O. Özcan,* M. F. Ünal,* A. R. Aslan,† Y. Bozkurt,‡ and N. H. Aydın‡
Istanbul Technical University, Maslak, Istanbul 80626, Turkey

Aerodynamic characteristics of external store configurations used on interceptor aircraft were investigated experimentally and computationally. Balance measurements, flow visualization, and static pressure measurements were made in a low-speed wind tunnel. The experimental and computational data revealed the global structure of the flow around a basic configuration. Six groups of models were used in the present study. This article discusses the results for the first and second group of models. The incompressible flow over a limited number of models was computed by solving the Navier-Stokes equations. The solution method is based on the Galerkin finite element discretization of space and the fractional step discretization of time. Reasonably good agreement was observed between the experimental and computational static pressure distributions on a basic geometry. The computational data, which revealed details of reverse flow regions, supported and supplemented the experimental data.

Introduction

MOST military stores are carried externally. External carriages facilitate the interchangeability of a wide range of stores and is often associated with a lower release disturbance than internal carriages.[1] An aircraft designed for external store carriage can be made smaller and lighter than an aircraft with an internal carriage. However, external carriages make a considerably large, twofold contribution to the total drag of a loaded aircraft: in addition to a drag of their own, external carriages cause an interference drag that depends on the installation arrangement. Reference 2 states that fighter aircraft designed before the 1970s tended to have very good aerodynamic cleanliness which, regrettably, stopped at the pylon. Today, however, aircraft manufacturers pay painstaking attention to the design of stores and carriages, and also to their compatibility with the aircraft body. Reduction of the interference drag is accomplished through modifications of the flow interactions between the store and the aircraft. On the other hand, minimization of external store drag involves selection of a proper form that eliminates major drag producing features.

In the present study, aerodynamic characteristics of an external bomb carriage were investigated experimentally and computationally. The carriage is currently used on the fighter aircraft of the Turkish Air Force. Experiments were conducted in a low-speed wind tunnel. Experimental data were obtained by balance measurements, flow visualization, and static pressure measurements. Thirty-four models, which were obtained by making systematic modifications to the carriage geometry, were used in the study. The models were divided into six different groups. This article presents the results for the first and second groups of models. Balance measurements for all of the six groups of models are discussed in a separate paper.[3] The incompressible Navier-Stokes equations were solved by using the Galerkin finite element method (in spatial discretization) and the fractional step method (in temporal discretization). Descriptions of the computational method can be found in Refs. 4–7. Successful test case computations by using the code employed in the present study are presented in Refs. 5–7. The scope of the study was limited to the aerodynamic characteristics of the isolated carriage, i.e., interference with the aircraft body was not investigated.

The experimental and computational data revealed the global structure of the flow around the carriage. Balance measurements showed that aerodynamically more suitable forms of the carriage geometry could be obtained by modifying its major drag-producing features. Surface flow visualization indicated locations of vortical flow regions whose existence was also supported by contour plots of the measured static pressure. Despite differences in the Reynolds numbers of the computed and measured flows, reasonably good agreement was observed between the experimental and computational static pressure distributions on the basic carriage geometry. The computations also exhibited details of reverse flow regions and, thus, both supported and supplemented the experimental data that did not include velocity measurements.

The geometry of the basic carriage used in the present study is not axisymmetric. There is a lack of data in the literature on studies of external stores that have nonaxisymmetric geometries. References 8 and 9 present data for bodies having square and rectangular cross sections. Studies of the flow around axisymmetric bodies show that there exist four characteristic flow regimes[10–12]: "vortex-free," "symmetric vortex," "asymmetric vortex," and "wake-like" flow regimes are observed with increasing angle of attack. Crossflow separation of the boundary layer on an axisymmetric body gives rise to formation of vortices on the lee side. Reference 10 states that the nonlinear lift force due to these vortices can be much larger than the lift predicted by the linear (small perturbation) theory. References 13–15 describe studies that investigate the effect of afterbody modifications on the drag of axisymmetric bodies. Interference between the flowfields of stores and aircraft bodies is investigated by Refs. 1 and 2.

Methodology

Experimental Setup and Models

Experiments were carried out in a low-speed subsonic wind tunnel having a cross-sectional area of 80 × 110 cm^2. The freestream velocity was kept constant at $V_\infty = 28.5 \pm 0.5$ m/s. At this flow speed, the freestream turbulence level was 0.2%. Reynolds number based on the model length varied in the range $1.06 \times 10^6 \leq Re \leq 1.34 \times 10^6$. On the other hand, Reynolds number based on the maximum diameter of model

Received Sept. 3, 1993; revision received Feb. 24, 1994; accepted for publication May 3, 1994.

*Professor, Faculty of Aeronautics and Astronautics.
†Associate Professor, Faculty of Aeronautics and Astronautics.
‡Research Assistant, Faculty of Aeronautics and Astronautics.

was 1.97×10^5. Angle of attack α was varied between -24 deg $\leq \alpha \leq 18$ deg.

Thirty four models, divided into six groups, were used in the study. Herein, experimental data will be presented for the first and second groups of models whose schematic descriptions are presented in Figs. 1 and 2. All of the dimensions are in millimeters. Model 1E represents the carriage geometry complete with four bombs and twin rocket-launchers. 1E is a one-quarter scaled-down model of the actual carriage used on aircraft. Models 1C and 1D are obtained by removing the bombs and rocket-launchers, respectively, from model 1E. 1A is the basic carriage geometry without bombs and rocket-launchers. Model 1B, which is an axisymmetric form of model 1A, is obtained by eliminating the step of model 1A at the end of the paraboloidal forebody. Model 1F is formed by using the paraboloidal forebody as an afterbody on model 1B. Rocket-launchers are hollow cylinders with a wall thickness of 0.5 mm and radius of 10 mm. A positive angle of attack α corresponds to a rotation of models in the clockwise direction in Figs. 1 and 2. The second group of models are generated by attaching seven different afterbodies on model 1A. The trailing-end thicknesses of the afterbodies are 25 mm for models 2A–2C, and 34 mm for models 2E–2G, respectively. The afterbody of model 2D is one-half of the paraboloidal forebody. The values of the boat-tail angles β for all second group models are given in Fig. 2.

Geometry of the paraboloidal forebody can be described by the following fourth-order polynomial with an accuracy better than 1%

$$(R/R_0) = -0.0436\eta^4 + 0.3155\eta^3 - 0.9625\eta^2 + 1.5079\eta + 0.0028 \quad (1)$$

where R is the radial location of the forebody surface in the symmetry plane, R_0 (50 mm) is the maximum radius of the paraboloidal forebody, and η is the normalized axial distance measured from the tip of model ($\eta = X/R_0$). An attempt was made to trip the boundary layer on the forebody by placing wires of 0.5 and 1.5 mm in diam at $X = 20$ mm. However, the trip-wires did not cause any observable effect on the static pressure distributions over the models. Therefore, it can be hypothesized that the laminar boundary layer developing on the forebody becomes transitional or turbulent before it reaches the step located at $X = 116$ mm.

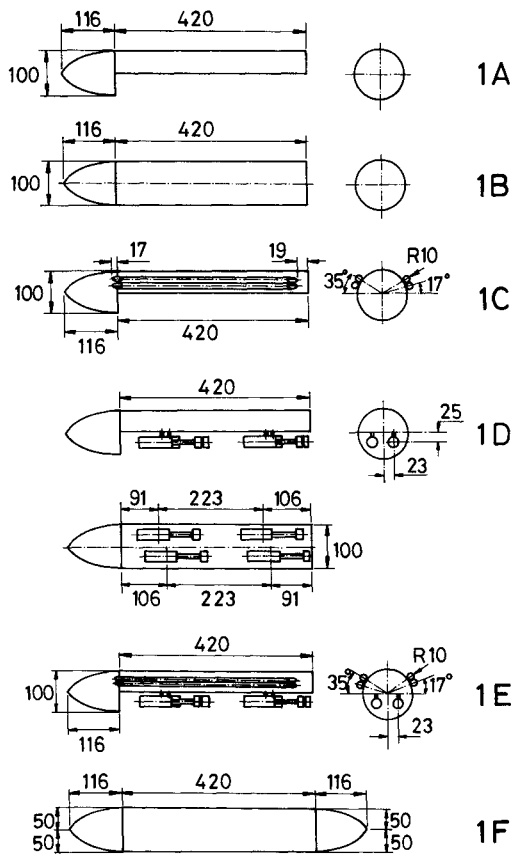

Fig. 1 Schematic drawings of the first group of models.

Experimental Technique

Prior to making modifications for drag reduction, flow visualization results were obtained for the basic model 1A at three different angles of attack, namely $\alpha = -15$, 0, and 15 deg. Topology of the friction lines on the model (i.e., separation and reattachment lines) were determined by the kerosene-lampblack technique,[16] which produced better results than the traditional surface oil flow visualization method. A video camera (SONY CCD-V600E) was used to record the skin-friction line patterns during tunnel runs. Topological interpretations of the skin-friction line patterns were made after careful and repeated examinations of the recordings. Additionally, information about the direction of the limiting streamlines were obtained by observing tufts attached to the model surface.

A three-component mechanical balance (Merrill) was used to measure the drag force D, the lift force L, and the pitching moment with respect to the balance center M_B. The measured forces and moments were converted into the axial A and normal N forces, and the pitching moment with respect to the body-tip M_0 by using Eqs. (2–4), which are given below:

$$A = D \cos \alpha - L \sin \alpha \quad (2)$$

$$N = D \sin \alpha + L \cos \alpha \quad (3)$$

$$M_0 = M_B - NX_B \quad (4)$$

where α is the angle of attack, and X_B (196 mm) is the axial distance between the tip of the model and the center of balance. Figure 3 shows a schematic drawing of the measured and derived forces and moments. X and X' are measured

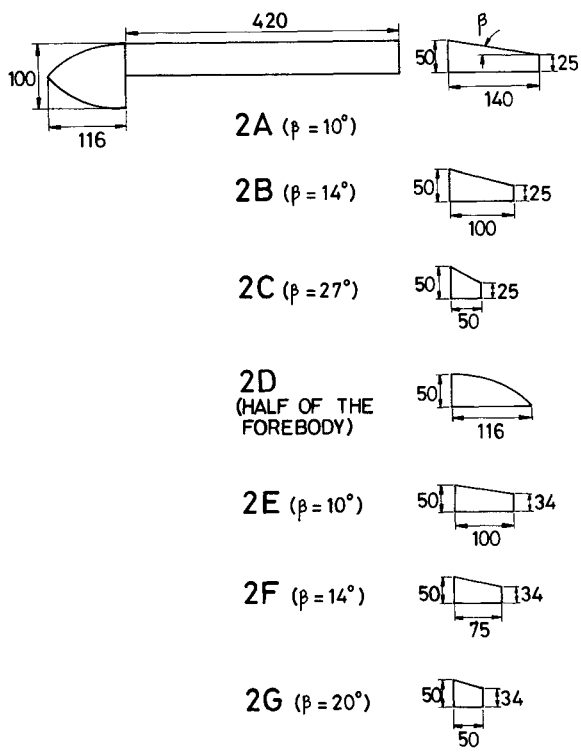

Fig. 2 Schematic drawings of the second group of models.

along the model axis and the freestream direction, respectively. The nondimensional coefficients C_A, C_N, C_{M0}, and the nondimensional pressure center location X^*_{CP} are calculated from Eqs. (5–8), which are given as

$$C_A = A/q_\infty S \tag{5}$$

$$C_N = N/q_\infty S \tag{6}$$

$$C_{M0} = M_0/q_\infty S l \tag{7}$$

$$X^*_{CP} = X_{CP}/l = (X_B/l) - (C_{MB}/C_N) \tag{8}$$

where $q_\infty = 0.5\rho_\infty V^2_\infty$ is the freestream dynamic pressure, and $S = \pi R_0^2$ is the maximum cross-sectional area of the paraboloidal forebody. l is the total length of the model including the afterbody. The nominal value of the freestream dynamic pressure is $q_\infty = 487$ N/m^2. Results presented here are the average values of the balance measurements repeated between three to four times. The uncertainties in C_A, C_N, C_{M0}, and X^*_{CP} are calculated by using an error analysis that is presented in Ref. 3. These uncertainties are given as follows: $\Delta C_A = \pm 0.080$, $\Delta C_N = \pm 0.095$, $\Delta C_{M0} = \pm 0.035$, and $\Delta X^*_{CP} = \pm 0.06$.

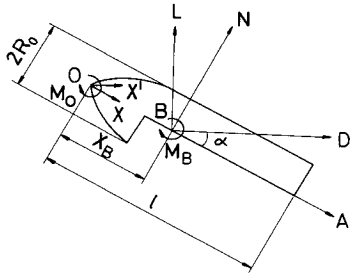

Fig. 3 Schematic drawing of the measured and derived forces and moments.

The paraboloidal forebody was instrumented with 24 pressure taps that were placed 5 mm apart in the axial X direction. The forebody could be rotated around the model axis so that this single line of pressure taps could be used to measure the static pressure p all around the forebody. The backward-facing step at the end of the forebody was also instrumented with 74 pressure taps that were located 5 mm apart in a square grid. There were 75 pressure taps spaced 10 mm apart in a square grid on the flat bottom part of model 1A between $116 < X$ (mm) < 266. Static pressures were measured by means of a multimanometer for various models at $\alpha = -15$, 0, and 15 deg. Data will be presented in terms of the static pressure coefficient that is defined as $C_P = 2(p - p_\infty)/\rho V^2_\infty$. The uncertainty in the pressure data is $\Delta p = \pm 1$ mm water $= \pm 0.02 q_\infty (\Delta C_P = \pm 0.03)$.

Computational Method

The incompressible, unsteady flow of a viscous fluid is governed by the Navier-Stokes and the continuity equations. In the absence of body forces, these are given by

$$\frac{\partial \boldsymbol{U}}{\partial t} + (\boldsymbol{U}\cdot\nabla)\boldsymbol{U} = -\nabla P + \frac{1}{Re}\nabla^2 \boldsymbol{U} \tag{9}$$

$$\nabla \cdot \boldsymbol{U} = 0 \tag{10}$$

where $\boldsymbol{U}$ is the velocity vector, Re is the Reynolds number, t is time, and P is the pressure. Note that all the variables are nondimensionalized by the freestream velocity V_∞ and the model length l. For the time derivative in Eq. (9), a finite difference representation (fractional step method) was employed. For the discretization of space, an integral finite ele-

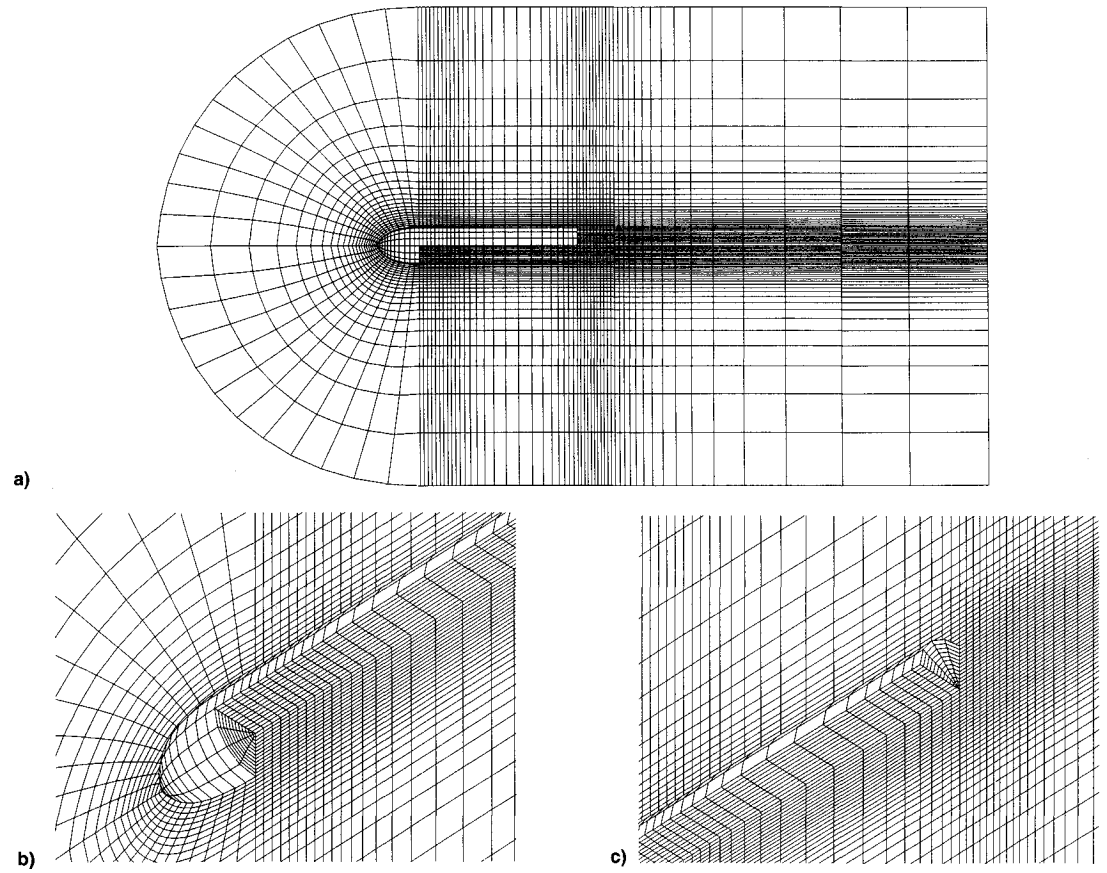

Fig. 4 Grid used in the computation of the laminar flow around model 1A: a) symmetry plane view, b) forebody grid detail, and c) trailing-edge grid detail.

ment formulation (Galerkin method) was used. The freestream values of velocity and pressure were taken as the initial conditions. Steady flow solutions were obtained at large times as an asymptotic state. The solution method is originally described in Ref. 4. Successful test case computations were presented by Refs. 5–7.

The fractional step velocity is defined by

$$\boldsymbol{U}^{m+1/2} = \boldsymbol{U}^m + \delta t[-\nabla P^m + (1/Re)\nabla^2 \boldsymbol{U}^m - (\boldsymbol{U}^m \cdot \nabla)\boldsymbol{U}^m] \tag{11}$$

where $\boldsymbol{U}^m$ and P^m are solutions at a known time level, and δt is the nondimensional time step. The velocity and pressure at a new time level ($\boldsymbol{U}^{m+1}$ and P^{m+1}) are calculated from

$$\boldsymbol{U}^{m+1} = \boldsymbol{U}^{m+1/2} + \nabla\phi \tag{12}$$

$$P^{m+1} = P^m - (\phi/\delta t) \tag{13}$$

where ϕ is a potential function solved from

$$\nabla^2\phi = -\nabla \cdot \boldsymbol{U}^{m+1/2} \tag{14}$$

For the spatial formulation of Eqs. (11–14) the Galerkin method was used. In this formulation eight-node isoparametric brick elements with trilinear interpolation functions for velocity and potential were utilized. Application of the Galerkin integral to the governing equations has given integral finite element formulations for one brick element.[4–7] On the surface of the body the no-slip boundary conditions for the velocity were given while the freestream values were retained far enough from the body.

Due to symmetry of the flow geometry with respect to the spanwise direction, computations were performed for one side of the symmetry plane where symmetry conditions[4–7] were applied. The grid used in the computation of the flow around model 1A at $\alpha = 0$ deg can be seen in Fig. 4. Figure 4a presents a symmetry plane view of the grid. Details of the grid near the forebody, step, and trailing edge are shown in Figs. 4b and 4c. The computational domain extends about one model length around the forebody and about two model lengths downstream from the trailing edge. The front half cylindrical part of the grid was generated by using an elliptic grid generator. The remaining straight part is generated algebraically. There were 16,596 grid points that formed 14,042 elements. A finer grid was chosen downstream of the step and the trailing edge in order to obtain details of the recirculating flow regions. The computations were performed on a personal computer equipped with a i860 RISC processor. The motion was started impulsively at time $t = 0$. The computation time for one time step was about 100 s. Small time steps had to be used in order to ensure stability of the explicit scheme employed in the study ($\delta t = 0.0015$). Results presented here were obtained for the nondimensional time of $t = 3$ (dimensional time of $3l/V_\infty$). Solutions did not change noticeably in the range of $2 < t < 5$. The computation time to reach $t = 5$ was approximately 90 h. The computations were performed for $Re = 1000$, which corresponded to the laminar flow regime. Turbulent flow calculations were not attempted due to limited capabilities of the computational facilities used in the study. Therefore, the computational and experimental data presented must be regarded as supplementary to each other in revealing the global structure of the flow.

Results and Discussion

Balance Measurements

Figure 5 gives the variation of the axial force coefficient C_A with angle of attack α for the first and second groups of models. Axially symmetric models 1F and 1B provide the minimum axial force among the first group of models (Fig. 5a). In comparison, the basic model 1A and the model with the launchers (1C) give axial forces that become increasingly larger for decreasing angle of attack. Even larger axial forces are obtained for the model with bombs (1D). Contributions of the bombs and the rocket-launchers to the axial force are not linear. The drag and axial forces are augmented more by the bombs than by the rocket-launchers. For small values of α, employment of afterbodies leads to a definite reduction in C_A of the basic model 1A (Figs. 5b and 5c). At large absolute values of angle of attack, the afterbodies become less effective in reducing the axial force. It may be noted that for bodies having axisymmetry (models 1B and 1F), the C_A variations are not exactly even functions of angle of attack (Fig. 5a). However, the deviations from the symmetry are smaller than the specified measurement uncertainties.

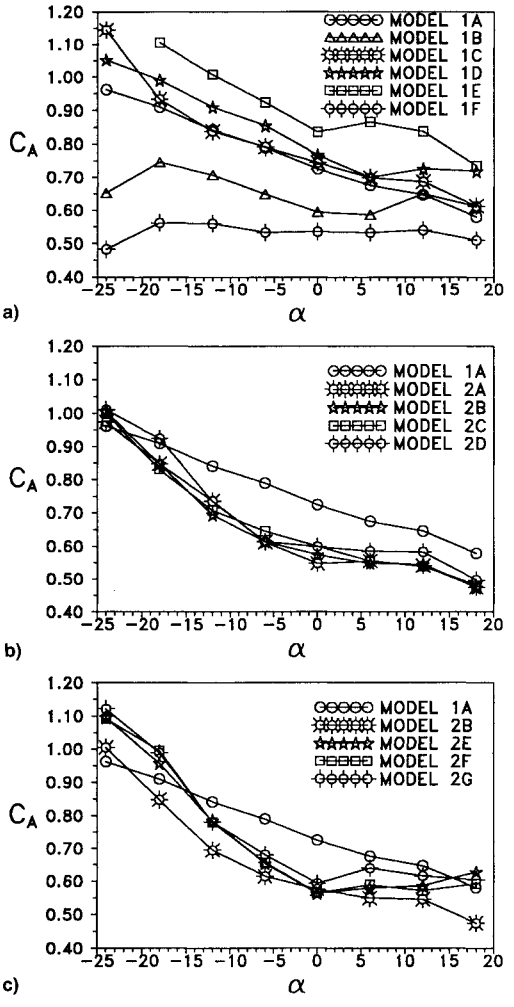

Fig. 5 Variation of C_A with α: a) first group of models and b), c) second group of models.

There exists a rough collapse of the data for models 2A–2C (Fig. 5b), and also for 2E–2G (Fig. 5c). This indicates that the base height of the half-cone afterbodies has a first-order effect on the aerodynamic characteristics. Results presented in Ref. 3 show that such a collapse of the balance data for afterbodies of the same base height does not occur when bombs are mounted on the models. Figure 5 shows that, for all nonaxisymmetric models, larger axial forces are associated with negative angles of attack. This implies existence of a wider wake region in the plane of symmetry for these angles. Derivative of the axial force coefficient with respect to the angle of attack (stability derivative $dC_A/d\alpha$) is quite small for the axisymmetric models (Fig. 5a). The balance data presented in Ref. 3 showed that the axial force acting on the

basic model 1A could be reduced further by making forebody modifications in addition to the afterbody modifications. However, a reduction of the axial force acting on model 1E (model complete with bombs and rocket-launchers) could not be accomplished by the forebody modifications reported in Ref. 3.

Figure 6 gives the variation of the normal force coefficient C_N with α for the first and second groups of models. Model 1C gives practically the same normal force as 1E (Fig. 6a). Similarly, C_N curves for models 1A and 1D are not much different. This leads to the conclusion that, the rocket-launchers, rather than the bombs, play a determining role in increasing the normal force. Naturally, the axially symmetric models 1F and 1B give a symmetric variation in the magnitude of the normal force. For the rest of the models, the variations deviate from the symmetry and result in larger forces for negative angles of attack. This indicates again the presence of a relatively wider separated flow region in the plane of symmetry for $\alpha < 0$ deg. C_N vs α curves for the second group of models are displaced upwards with respect to that of the basic model 1A (Figs. 6b and 6c). The amount of displacement increases slightly with increasing α.

Figure 7 shows the variations of the pitching moment coefficient C_{M0} and the normalized pressure center location $X^*_{CP} = X_{CP}/l$ with angle of attack for some of the models in the first and second groups. C_{M0} and X^*_{CP} data for all models are presented in Refs. 3 and 17. C_{M0} decreases monotonically with increasing α for all nonaxisymmetric models (Fig. 7a). The effect of afterbodies mounted on model 1A is to decrease C_{M0} by an approximately constant amount. The effect of afterbodies on X^*_{CP} is most significant at negative angles of attack (Fig. 7b). In this case, the pressure center moves in the upstream direction with increasing α for all models in the second group. At the limiting angles of attack, the approximate values of the pressure center location are $X^*_{CP} \cong 0.25$ ($\alpha = -24$ deg) and $X^*_{CP} \cong 0.45$ ($\alpha = 18$ deg). Indefinite values of the pressure center X^*_{CP} in the neighborhood of $\alpha = 0$ deg, which are calculated as the normal force coefficient goes to zero, are not shown in Fig. 7b.

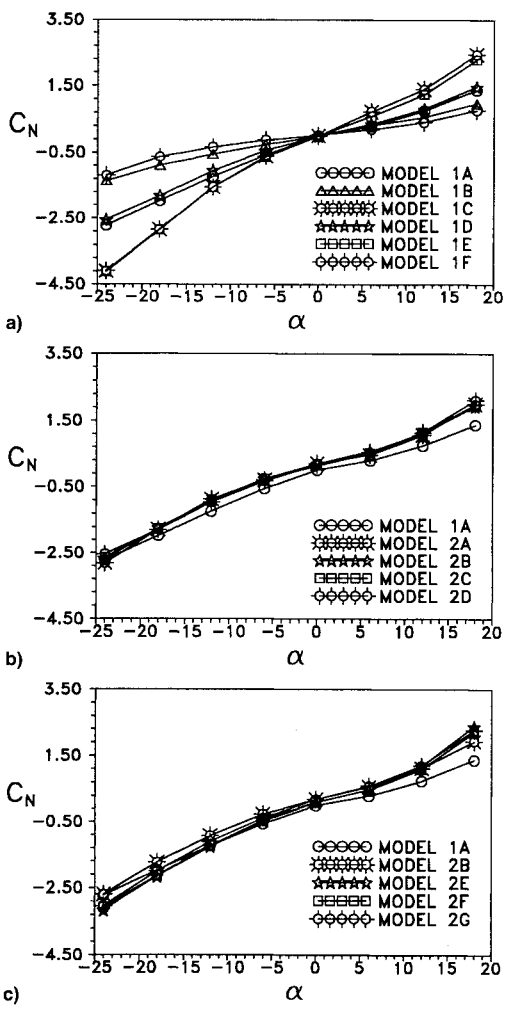

Fig. 6 Variation of C_N with α: a) first group of models and b), c) second group of models.

Flow Visualization

Figures 8 and 9 show schematic descriptions of the skin-friction line topology on model 1A at $\alpha = 15$ deg and $\alpha = -15$ deg, respectively. Surface shear stress vector is tangent to the skin-friction lines observed by surface flow visualiza-

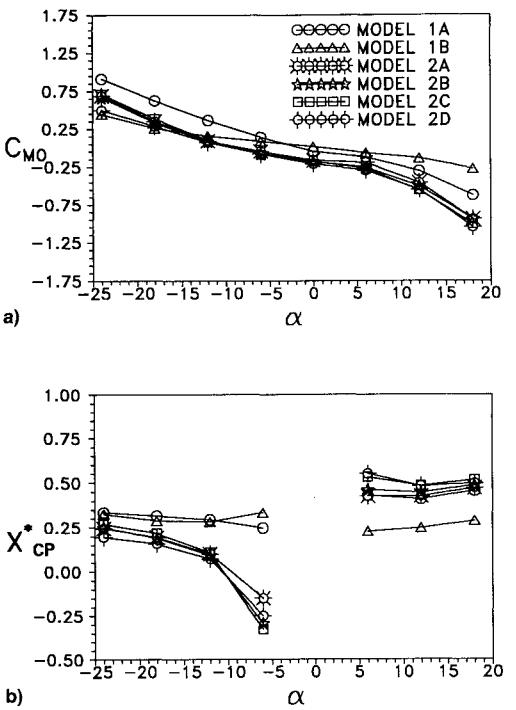

Fig. 7 Variations of a) C_{M0} and b) (X^*_{CP}) with α.

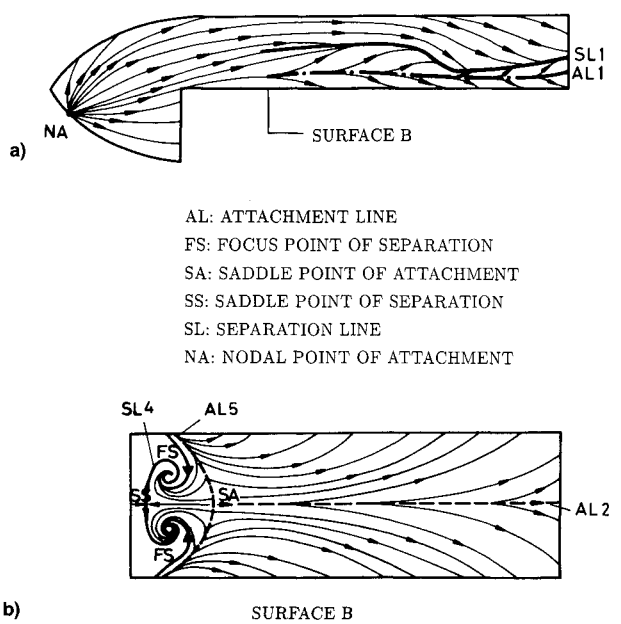

Fig. 8 Skin-friction line patterns on model 1A at $\alpha = 15$ deg: a) surface C and b) surface B.

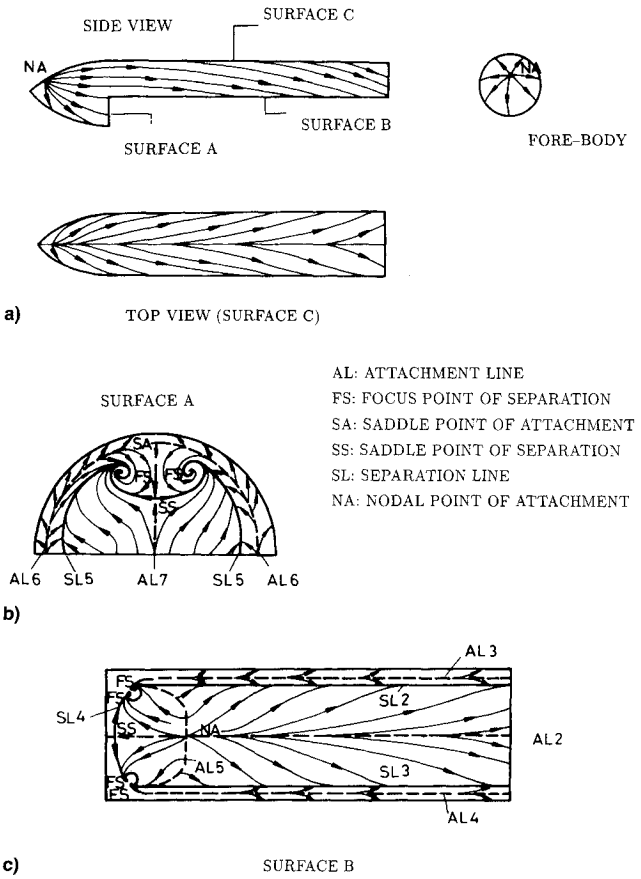

Fig. 9 Skin-friction line patterns on model 1A at $\alpha = -15$ deg: a) surface C, b) surface A, and c) surface B.

tion. Three-dimensional flow separation and topology of the skin-friction lines have recently been discussed by Hung.[18] The terminology of Tobak and Peake,[19] who state that a necessary condition for the occurrence of flow separation is the convergence of skin-friction lines onto a particular line, is used in this article. An attachment line is a skin-friction line along which there exists a divergence of all other skin-friction lines. In Figs. 8 and 9, separation and attachment lines are indicated by thick continuous and dashed lines denoted by letters SL and AL, respectively. Shear stress is zero only at the singular points of NA, SA, SS, and FS. Surfaces A, B, and C denote the step at the end of the paraboloidal forebody, the bottom of the carriage, and the top of the model, respectively. Surface A is a half-circle, whereas surface B is a rectangle. Surfaces A and B are flat, whereas surface C is a half-cylinder. It should be noted that experimentally observed skin-friction line patterns may sometimes be interpreted in more than one unique way. The topological interpretations given herein omit fine details and describe the salient features of the surface flow.

Figure 8a shows the presence of a crossflow separation line (SL1) and an attachment line (AL1) on the upper surface (surface C) of model 1A at $\alpha = 15$ deg. SL1 is a local (open) separation line that originates from a noncritical point on surface C. As shown in Fig. 9a, SL1 and AL1 do not exist at $\alpha = -15$ deg. For the latter case, the surface flow is deflected downwards and separates inviscidly from the sharp edge of surface C. SL1 and AL1 were not observed at zero angle of attack either. According to the definition of Ref. 11, the basic structure of the flow over axisymmetric bodies is "vortex-free" type around $\alpha = 0$ deg, and "symmetric vortex" type in the approximate range of 10 deg $\leq \alpha \leq 30$ deg. Present results indicate that the flow over model 1A is symmetric vortex type at $\alpha = \pm 15$ deg. Any concrete evidence of crossflow could not be found by flow visualization at $\alpha = 0$ deg. However, the computational results indicated that the flow over model 1A is not of vortex-free type, even at zero angle of attack.

The boundary layer developing on the paraboloidal forebody of model 1A separates inviscidly from the sharp edge of the step denoted as surface A. The separating flow reattaches on surface B along the attachment line AL5 that is shown in Fig. 8b. Comparison of Figs. 8b and 9c shows that topology of the skin-friction lines on surface B varies with angle of attack. There exist two separation lines (SL2 and SL3) and three attachment lines (AL2, AL3, and AL4), which are all parallel to the model axis, on surface B at $\alpha = -15$ deg. The model axis on surface B becomes a line of reattachment (AL2) for the flow separating inviscidly from the sharp corner of surface C (Fig. 9c). Due to adverse pressure gradients on surface B, the crossflow separates along SL2 and SL3, and reattaches along AL3 and AL4. The secondary flow vortices generated by these viscous separations are smaller than the primary vortices formed by inviscid separation from the sharp edge of surface C.

As α increases from -15 to 0 deg, SL2, SL3, AL3, and AL4 approach the sharp edge of surface B and disappear. The topology of the skin-friction lines on surface B does not change in the range of 0 deg $\leq \alpha \leq 15$ deg. Figures 8b and 9c show that on surface B the reverse flow approaching the step separates along SL4, which is a global separation line originating from a saddle-point singularity. It may be hypothesized that FS singular points are footprints of tornado vortices that rise perpendicularly to surface B before they bend 90 deg and become longitudinal vortices.

Figure 9b shows the skin-friction line pattern on the step (surface A). This pattern involves a global separation line (SL5) and two attachment lines (AL6 and AL7). AL7 lies in the plane of symmetry. Due to very small magnitude of the shear stress levels on surface A, the skin-friction line topology at $\alpha = 0$ and 15 deg could not be determined with sufficient accuracy. The symmetrically positioned FS singular points on surface A are presumed to be the footprints of two counter-rotating vortices.

Figures 10a and 10b give the postulated crossflow streamline patterns near the trailing edge of model 1A at $\alpha = 15$ deg and $\alpha = -15$ deg, respectively. These patterns are compatible with the flow visualization results and must be considered as time-averaged streamline patterns. For the sake of clarity, the tornado vortices that originate from surfaces A and B are not shown in Fig. 10. S1, S2, F1, F2, F3, and F4 are the singular points of the crossflow velocity field. Saddle and focus points are denoted by S and F, respectively. The vortices at points F2 and F4 are generated by viscous separation of boundary layers developing on the model. On the other hand, inviscid separation of the flow from the sharp corner gives rise to the formation of the vortices at F1 and F3. Since the separating flow must be approximately tangent to the body during the formation of F1 and F3, the wake region of crossflow must be larger at $\alpha = 15$ deg than that at $\alpha = -15$ deg.

Static Pressure Measurements

Figure 11 shows the variation of the calculated and measured C_p along the axis of model 1A at $\alpha = 0$ deg. $X^* = X/l$ is the normalized distance measured along the line of symmetry. C_p decreases steeply as the flow accelerates on the paraboloidal forebody. The experimental data show the presence of an adverse pressure gradient region in the range of $0.15 \leq X^* \leq 0.28$. The pressure distributions given by Ref. 20 also reveal adverse pressure gradient regions on the ellipsoidal and spheroidal forebodies of axisymmetric objects. For $X^* \geq 0.3$, C_p does not change significantly with X^*. Despite the differences in the Reynolds number, the agreement between the experimental and computational results is generally good. This result is not surprising because the flow is stream-

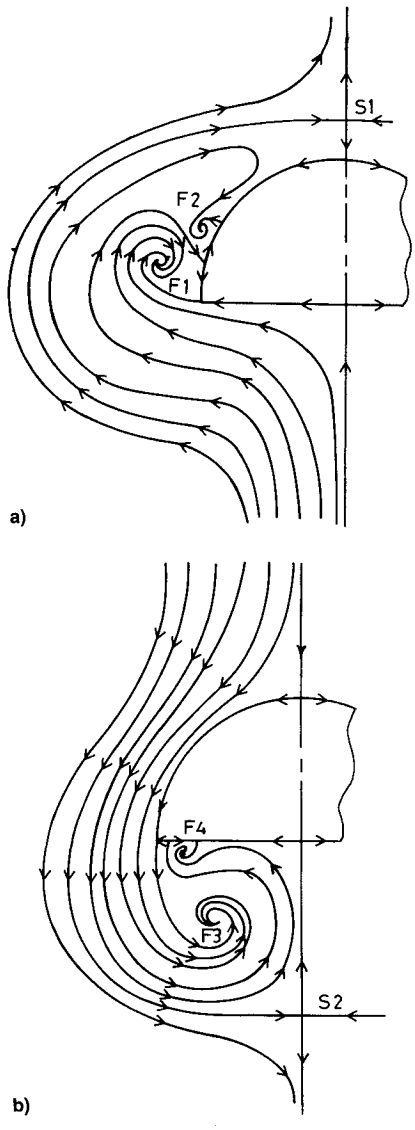

Fig. 10 Posulated streamline patterns in the crossflow planes near the trailing edge for model 1A: a) α = 15 deg and b) α = −15 deg.

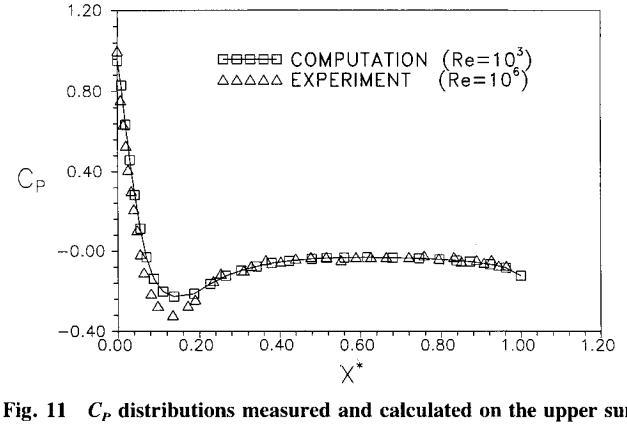

Fig. 11 C_P distributions measured and calculated on the upper surface of model 1A along the axis of symmetry at α = 0 deg.

lined and viscous effects are minimum on the upper surface of model 1A at α = 0 deg.

Figure 12 gives the variations of C_P measured on the upper and lower surfaces of model 1A along the line of symmetry at α = −15, 0, and 15 deg. On the upper surface, the adverse pressure gradient region is larger at α = 15 deg than that at α = 0 deg. The adverse pressure gradient weakens with decreasing α and disappears at α = −15 deg. For $X^* \geq 0.3$,

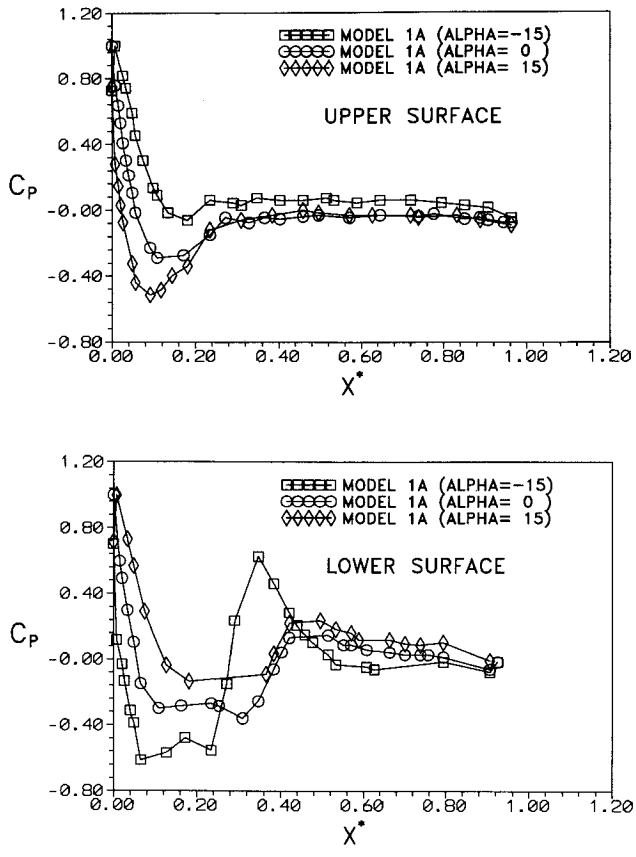

Fig. 12 C_P distributions measured on the upper and lower surfaces of model 1A along the axis of symmetry at α = −15, 0, and 15 deg.

upper surface C_P values remain constant along the model and change slightly with angle of attack. For the lower surface, the adverse pressure gradient on the forebody is rather small. The step on the bottom of model 1A is located at $X^* = 0.22$. Downstream of the step on surface B (lower surface), C_P first decreases and then increases with increasing X^*. C_P values reach a maximum around the singular point of reattachment. For larger X^* values, C_P distributions approach plateau values that do not change significantly with α. The pressure distribution on surface B (lower surface), which is very similar for α = 15 and 0 deg, changes significantly with angle of attack as α decreases to −15 deg. The location of maximum C_P, which is around $X^* = 0.46$ at α = 0 and 15 deg, moves to $X^* = 0.33$ at α = −15 deg. The values of the maximum C_P downstream of the step are 0.20, 0.28, and 0.68 at α = 15, 0, and −15 deg, respectively.

Figure 13 gives contour plots of C_P measured on the forebody of the basic model 1A at angles of attack of α = −15 and 15 deg. Data are shown on side views of the model in the range of $0 \leq X$ (mm) ≤ 101. Pressure taps are located at radial locations of $R \cos \varphi$ for all roll angles (φ), except for φ = 0 and 180 deg (plane of symmetry). In order to avoid overcrowding of the measurement grid, the data for the roll angles of φ = 0 deg and φ = 180 deg (the lee side and the wind side, respectively, at positive angles of attack), are shown at radial locations of $R(1 + \cos 15 \text{ deg})$, i.e., the boundary of the forebody is displaced by R cos 15 deg from its real position. Variation of C_P between adjacent curves is 0.1. C_P is equal to 1 at the stagnation point that is located off the model axis for nonzero angles of attack. The constant pressure lines are roughly parallel to each other and inclined at angles of approximately ±55 deg with respect to the X axis near the model tip. The pressure contours at α = ±15 deg show a remarkably good degree of symmetry with respect to each other. This result indicates that the pressure field on the

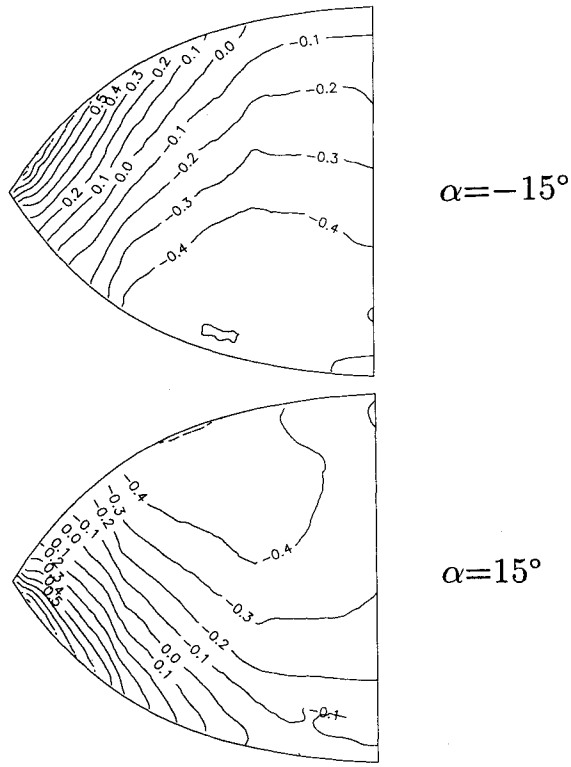

Fig. 13 Contour plots of C_P measured on the forebody of the model 1A at $\alpha = -15$ and 15 deg.

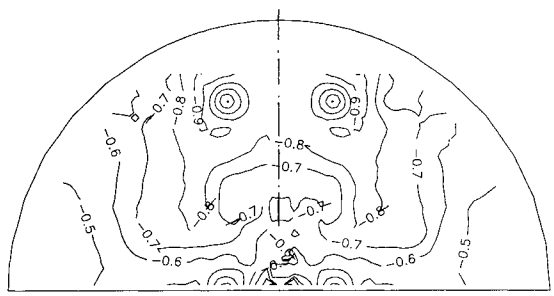

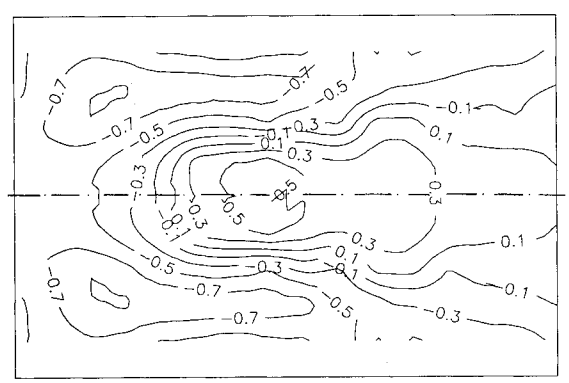

Fig. 14 Contour plots of C_P measured on surface A and surface B of model 1A at $\alpha = -15$ deg.

forebody is not influenced significantly by the step located at $X^* = 0.22$.

Figure 14 shows contour plots of the static pressure coefficient measured on the step surface (surface A) and the flat lower surface (surface B) of model 1A at $\alpha = -15$ deg. C_P varies by 0.1 and 0.2 between adjacent contours on surface A and surface B, respectively. Static pressures were measured on one side of the symmetry plane ($\varphi = 0$ deg) and symmetry was assumed in plotting Fig. 14. Data are shown between 0.22

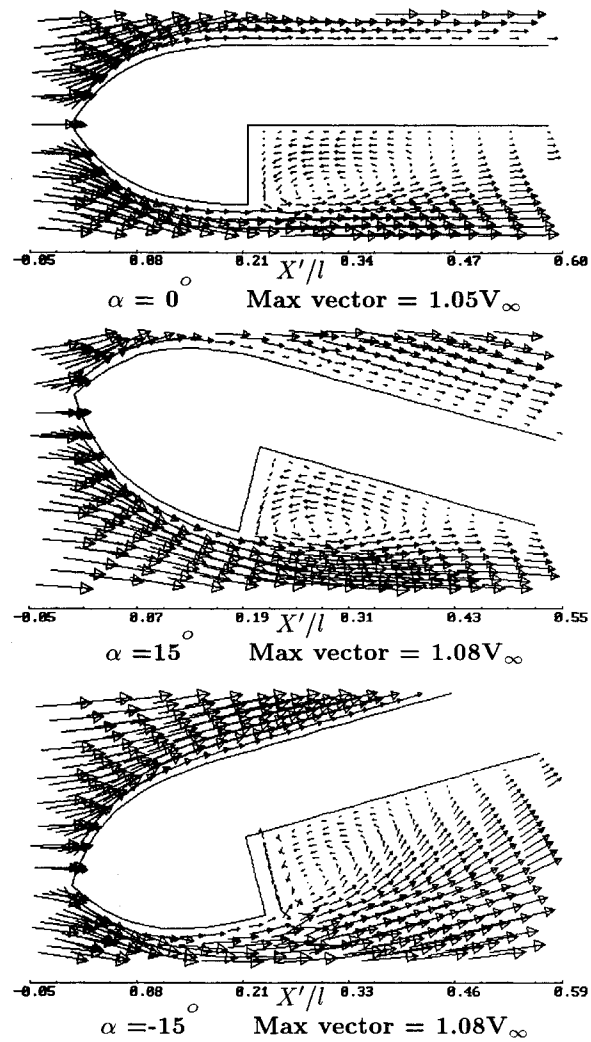

Fig. 15 Computed velocity vector field on the plane of symmetry near the forebody of model 1A at angles of attack of $\alpha = 0$, 15, and -15 deg.

$< X^* < 0.50$ on surface B. The circular contours near the top of surface A are thought to be related to the tornado vortices, the footprints of which are the focus points of separation (FS) in Fig. 9. On surface A, C_P increases from -0.9 to -0.6 as the centers of the circles are approached. On surface B, there exist significantly large pressure gradients, not only in the streamwise, but also in the spanwise direction.

Computed Flowfield

Figure 15 shows the computed velocity vector field on the plane of symmetry near the forebody of model 1A at angles of attack of $\alpha = 0$, 15, and -15 deg. Magnitudes of the maximum velocity vectors are also indicated. The size of the reverse flow region downstream of the step L_1 was determined from an analysis of the computational data. L_1 was measured along the axis of symmetry between the step and the reattachment point on surface B. The normalized reverse flow size $L_1^* = L_1/l$ was approximately equal to 0.25 for $\alpha = 0$, 15, and -15 deg. The uncertainty in determining L_1^* is estimated to be $\Delta L_1^* = \pm 0.02$.

Figure 16 gives the computed velocity vector field on the plane of symmetry near the trailing edge of model 1A at angles of attack of $\alpha = 0$, 15, and -15 deg. The size of the reverse flow region in the wake L_2 is determined by using the computational data. Figure 17 shows the postulated streamline patterns in the wake region of model 1A at angles of attack of $\alpha = 0$, 15, and -15 deg. The postulated streamline patterns involve a saddle type of singular point (S) where velocity

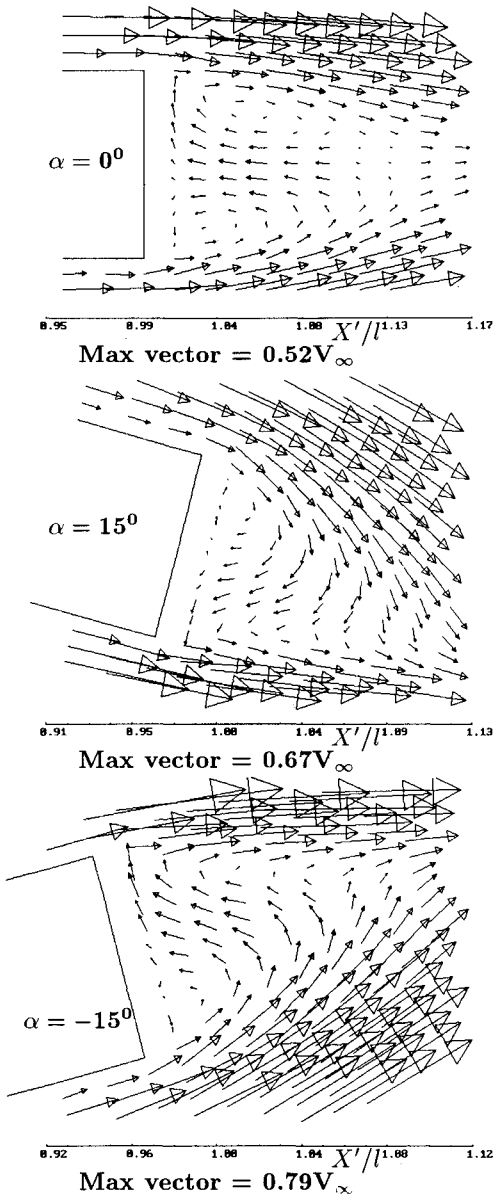

Fig. 16 Computed velocity vector field on the plane of symmetry near the trailing edge of model 1A at angles of attack of α = 0, 15, and −15 deg.

vector is zero. It must be noted, however, that alternative streamline patterns that do not include a saddle point of singularity may also be postulated.[21] In Fig. 17, S′ is the reattachment point on the base of the model, and points F are focus type singularities in the streamline pattern. L_2 is measured between the trailing edge and the saddle point S along the X axis. The normalized size of the reverse flow region in the wake ($L_2^* = L_2/l$) is equal to 0.13 at α = 0 deg, and to 0.10 at $\alpha = \pm 15$ deg, respectively. The uncertainty in determining L_2^* is estimated to be $\Delta L_2^* = \pm 0.02$. It can be argued that, at zero angle of attack, the reverse flow region is longest because it is hidden completely from the freestream. Evidently, the reverse flow region shrinks with increasing angle of attack as it becomes exposed to high kinetic energy of the outer flow. In Fig. 17, two counter-rotating spanwise vortices can be seen around foci F. These vortices are of approximately equal size at zero angle of attack. At α = 15 deg, the vortex near the top of the carriage (φ = 0 deg) is larger than the vortex near the bottom part (φ = 180 deg). On the other hand, at α = −15 deg, the bottom vortex is larger than the top vortex. In both cases, the larger vortex is located on the lee side.

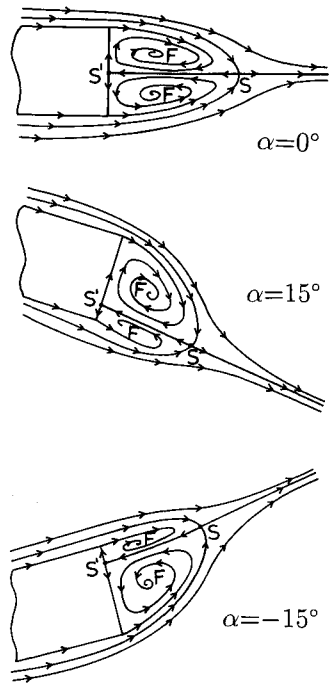

Fig. 17 Postulated streamline patterns in the wake region of model 1A at angles of attack of α = 0, 15, and −15 deg.

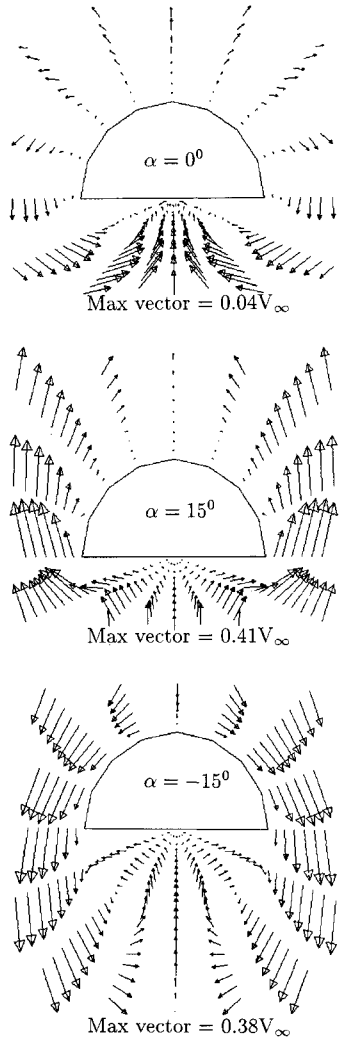

Fig. 18 Computed velocity vector field of the crossflow at X^* = 0.64 on model 1A for α = 0, 15, and −15 deg.

Figure 18 shows the computed velocity vector field of the cross flow at $X^* = 0.64$ on the basic model 1A for $\alpha = 0$, 15, and -15 deg. Magnitudes of the maximum velocity vectors are indicated on the figure. The semicircular shape of the body is approximated by a six-sided polygon in the computational grid. The computation reveals a pair of counter-rotating streamwise vortices for all angles of attack. Thus, the flow at $\alpha = 0$ deg is not of vortex-free type in contrast to the case of axisymmetric geometries. It can be argued that the counter-rotating vortices are generated by separation from the sharp edge of the body, i.e., they are the vortices located around points F1 and F3 in the postulated streamline pattern given by Fig. 10. The postulated vortices located around points F2 and F4 in Fig. 10 are not predicted by the computation. This is possibly due to the limited resolution of the grid in the azimuthal direction. Hung[18] demonstrates that grid resolution can affect the calculated topology of the surface flow.

Computational results presented in Ref. 17 showed that the size of the reverse flow region in the base of model 2B was considerably smaller than that of model 1A at $\alpha = 0$ deg. Experimental data reported in Ref. 17 also revealed that static pressure distributions on the lower and upper surfaces of models 1A and 2B were virtually identical. Thus, it could be speculated that the drag reduction observed for model 2B was mainly due to the decrease of reverse flow region downstream of the trailing edge.

Conclusions

1) The rocket-launchers played a determining role in increasing the normal force acting on the basic model 1A. The drag and axial forces were augmented more by the bombs than by the rocket-launchers.

2) For all nonaxisymmetric models, the drag and the axial forces were found to be larger at negative angles of attack, which indicated the existence of a wider wake region in the plane of symmetry for $\alpha < 0$ deg.

3) Balance measurements showed that aerodynamically more suitable forms of the carriage geometry could be obtained by modifying its major drag-producing features. Models 2A and 2B gave the minimum drag and axial force. There was a rough collapse of the data for models 2A–2C, and also for 2E–2G. This indicated that the base height of the half-cone afterbodies had a first-order effect on drag, lift, and pitching moment.

4) For all nonaxisymmetric models, the pitching moment around the model tip M_0 decreased monotonically with increasing α. The effect of afterbodies on X^*_{CP} was most significant at negative angles of attack for which the pressure center moved upstream with increasing α.

5) Good agreement was observed between the static pressures measured and calculated along the axis of model on the upper surface (surface C) of model 1A.

6) Flow visualization results for model 1A indicated the existence of large-scale and small-scale counter-rotating streamwise vortices. It was hypothesized that the large-scale vortices were generated by inviscid flow separation from the sharp edges of the body, whereas the small-scale vortices were formed by the crossflow separation of the boundary layer.

7) Computation of the flow around model 1A confirmed existence of the postulated large-scale streamwise vortices. However, the postulated small-scale streamwise vortices could not be predicted by the computation. Computations also showed that the flow was not of vortex-free type, even at $\alpha = 0$ deg.

8) The experimental and computational data presented herein supported and supplemented each other in revealing the global structure of the flow around the basic model 1A.

Acknowledgments

This study was supported by a grant from the Turkish Air Force "First Air Supply Base," Eskisehir, Turkey. A. N. Yüksel and F. Aydınmakina were the project managers. The assistance of A. Doğan and B. K. Yüceil in the experimental and of F. O. Edis in the computational parts of the study are gratefully acknowledged. We would also like to thank A. Şalcı for his design of the basic model, and the reviewers of this article for their valuable suggestions and comments.

References

[1]Hugh, P. G., and Hutton, P. G., "The Drag of Externally Carried Stores—Its Prediction and Alleviation," *Aerodynamic Drag*, AGARD CP-124, Oct. 1973.

[2]Bore, C. L., "Airframe/Store Compatibility," *Fundamentals of Fighter Aircraft Design*, AGARD-FDP-VKI Special Course, Feb. 1986.

[3]Özcan, O., Ünal, M. F., Bozkurt, Y., and Doğan, A., "Aerodynamic Characteristics of an External Store Carriage: Part B," AIAA Paper 94-0289, Jan. 1994.

[4]Mizukami, A., and Tsuchiya, M., "Finite Element Method for the 3-D Non-Steady Navier-Stokes Equations," *International Journal for Numerical Methods in Fluids*, Vol. 4, No. 4, 1984, pp. 349–357.

[5]Gülçat, Ü., and Gürgey, E., "A Zonal Approach in Solving 3D Unsteady Viscous Flows via FEM," *Proceedings of the 7th International Conference on Finite Element Methods in Flow Problems*, AL, 1988.

[6]Aslan, A. R., Edis, F. O., Gülçat, Ü., and Gürgey, E., "Prediction of General Viscous Flows Using a Finite Element Method," *Proceedings of the 8th International Conference on Numerical Methods in Laminar and Turbulent Flows*, Pineridge Press International, Swansea, Wales, UK, 1993, pp. 655–667.

[7]Gürgey, E., Aslan, A. R., Edis, F. O., and Gülçat, Ü., "3D Finite Element Computation of Unsteady General Viscous Flow," *Proceedings of the 8th International Conference on Finite Elements in Fluids, New Trends and Applications*, edited by K. Morgan, E. Oñate, J. Periaux, J. Peraire, and O. C. Zienkiewicz, CIMNE/Pineridge Press, Barcelona, Spain, 1993, pp. 184–193.

[8]Sigal, A., and Lapidot, E., "Aerodynamic Characteristics of Configurations Having Bodies with Square, Rectangular and Circular Cross Sections," *Journal of Spacecraft and Rockets*, Vol. 26, No. 2, 1989, pp. 85–89.

[9]Daniel, D., Yechout, R., and Zollars, G., "Experimental Aerodynamic Characteristics of Missiles with Square Cross Sections," *Journal of Spacecraft and Rockets*, Vol. 19, No. 2, 1982, pp. 167–172.

[10]Peake, D. J., and Tobak, M., "Three-Dimensional Flows About Simple Components at Angle of Attack," *High Angle of Attack Aerodynamics*, AGARD LS-121, Dec. 1982.

[11]Keener, E. R., "Oil Flow Separation Patterns on an Ogive Forebody," *AIAA Journal*, Vol. 21, No. 4, 1983, pp. 550–556.

[12]Ward, K. C., and Katz, J., "Topology of the Flow Structures Behind as Inclined Projectile: Part A," *Journal of Aircraft*, Vol. 26, No. 11, 1989, pp. 1016–1022.

[13]Kentfield, J. A. C., "Short, Multi-Step, Afterbody Fairings," *Journal of Aircraft*, Vol. 21, No. 5, 1984, pp. 351, 352.

[14]Kidd, J. A., Wikoff, D., and Cottrell, C. J., "Drag Reduction by Controlling Flow Separation Using Stepped Afterbodies," *Journal of Aircraft*, Vol. 27, No. 6, 1990, pp. 564–566.

[15]Xia, X. J., and Bearman, P. W., "An Experimental Investigation of the Wake of an Axisymmetric Body with a Slanted Base," *Aeronautical Quarterly*, Vol. 34, Pt. 1, Feb. 1983, pp. 24–45.

[16]Settles, G. S., and Teng, H. Y., "Flow Visualization Methods for Separated Three-Dimensional Shock-Wave Turbulent Boundary-Layer Interactions," *AIAA Journal*, Vol. 21, No. 3, 1983, pp. 390–397.

[17]Özcan, O., Ünal, M. F., Aslan, A. R., Bozkurt, Y., and Aydın, N. H., "Aerodynamic Characteristics of an External Store Carriage: Part A," AIAA Paper 93-3507, Aug. 1993.

[18]Hung, C. M., "Computation of Navier-Stokes Equations for Three-Dimensional Flow Separation," *AIAA Journal*, Vol. 29, No. 10, 1991, pp. 1659–1667.

[19]Tobak, M., and Peake, D. J., "Topology of Three-Dimensional Separated Flows," *Annual Review of Fluid Mechanics*, Vol. 14, 1982, pp. 61–85.

[20]Larson, E. S., "Low Speed Pressure Distribution on Axisymmetric Elliptic-Nosed Bodies," *Journal of Aircraft*, Vol. 25, No. 10, 1988, pp. 969, 1970.

[21]Delery, J., and Lacau, R. G., "Prediction of Base Flows," *Special Course on Missile Aerodynamics*, AGARD-R-754, April 1988.